Accepted to Phys. Fluids 10.1063/5.0187608

Transient thermocapillary convection under a surface of a linear temperature distribution

Xinyuan Meng (孟欣湲)[1], Enhui Chen (陈恩惠)[1, a)], Feng Xu (徐丰)[1]

[1]*School of Physical Science and Engineering, Beijing Jiaotong University, Beijing 100044, China*

[a)] Author to whom correspondence should be addressed: ehchen@bjtu.edu.cn

ABSTRACT Transient thermocapillary convection under a surface of a linear temperature distribution in a top open cavity at a zero-gravity condition is investigated using scaling analysis and numerical simulation. Induced by the linear temperature distribution on a surface, a surface flow (SF) occurs. Then the pressure gradient near the sidewall drives a vertical flow (VF). The evolution in dynamics and heat transfer of the SF and the VF is argued, which is determined by Marangoni number (*Ma*), Prandtl number (*Pr*) and aspect ratio (*A*). Scaling analysis shows that there are four typical evolutions of the VF and two typical evolutions of the thermal boundary layer (TBL). Further, velocity, boundary layer thickness, and Nusselt number of transient thermocapillary convection are scaled under different regimes in different evolutions and a number of new scaling laws are proposed. Additionally, the flow structures under different regimes are characterized and selected scaling laws obtained in scaling analysis are validated by numerical simulation results.

KEYWORDS: transient thermocapillary convection, linear temperature distribution, scaling analysis, numerical simulation

NOMENCLATURE

A	aspect ratio
A_ε	aspect ratio of surface layer
c_p	specific heat of working fluid ($Jkg^{-1}K^{-1}$)
F_α	thermocapillary force (ms^{-2})
H	height of cavity (m)
k	temperature gradient factor (Km^{-1})
L	length of cavity (m)
Ma	Marangoni number
Nu	Nusselt number
p	pressure ($kgm^{-1}s^{-2}$)
Pr	Prandtl number
Q	flow rate (m^3s^{-1})
Q_i, Q_v, Q_s	flow rate of VF (m^3s^{-1})
t	time (s)
t_i, t_t, t_{ts}, t_H	transition time of SF under different regime (s)
T	temperature (K)
T_0	temperature of working fluid at initial time (K)
u, v	velocities in x- and y-directions (ms^{-1})

u_i, u_v, u_s	velocity of SF under different regime (ms^{-1})
v_{ii}, v_{iv}, v_{Hi}, v_{HH}, v_{Hv}, v_{vi}, v_{vv}, v_{vH}	velocity of VF under different regime (ms^{-1})
x, y	coordinates in x- and y-directions (m)
Greek symbols	
*	nondimensional variables such as ε^*, p^*, u^*, t^* and x^*
α	surface tension (Nm^{-1})
α_T	temperature coefficient of surface tension ($Nm^{-1}K^{-1}$)
β	coefficient of thermal expansion (K^{-1})
δ	Dirac delta-function (m^{-1})
δ_{Ti}, δ_{Tv}, δ_{Ts}	thickness of TBL under different regime (m)
δ_v	thickness of viscous boundary layer (m)
Δ	thickness of VF (m)
Δ_{ii}, Δ_{iv}, Δ_{Hi}, Δ_{HH}, Δ_{Hv}, Δ_{vi}, Δ_{vv}, Δ_{vH}	thickness of VF under different regime (m)
ΔT	temperature difference between two ends of surface (K)
ε	thickness of surface layer (m)
κ	heat diffusivity (m^2s^{-1})
λ	heat conductivity ($Wm^{-1}K^{-1}$)
ν	viscosity (m^2s^{-1})
ρ	density (kgm^{-3})
τ_{vi}, τ_{vHv}, τ_{Hi}, τ_{vv}, τ_{Hv}, τ_{HH}	transition time of VF under different regime (s)

I. INTRODUCTION

A temperature gradient is common on liquid surface in nature and industrial systems, which induces a nonuniform surface tension on liquid surface in which the maximum tension can arise in the coldest region of the surface ($\alpha_T = -\mathrm{d}\alpha/\mathrm{d}T > 0$, see Refs. 1, 2). Such a nonuniform tension may further "drag" the liquid flow, which is known as thermocapillary convection.[3] Thermocapillary convection exists in many practical applications such as laser surface melting and alloying,[4] the crystal fabrication,[5] 3D-printing technology,[6] the purification of carbon nanotubes[7] and micromanipulation.[8]

The study of thermocapillary convection has received increasing attention over the past decades.[9, 10] Recently, thermocapillary convection in a shallow liquid film with two gas-liquid interfaces,[11] a liquid bridge of various Prandtl numbers (Pr),[12] a rectangular liquid cavity with an isothermal sidewall,[13] a cylindrical liquid pool,[14] a cylindrical cell with a bidirectional temperature gradient,[15] an annular two-layer system,[16] or a planar droplet[17, 18] has been investigated using theory, simulation and experiment on the earth and in space. Further, more attention has been paid into the effect of gravity,[19] evaporation,[20, 21] surface deformation,[22] phase change,[23] gas flow[24] and instability on thermocapillary convection.[25-27]

Many interests have also been devoted to thermocapillary convection in a rectangular side-heated top open cavity. The effect of gravity on thermocapillary convection has been studied for various liquids and geometry sizes by linear stability analysis,[28] numerical simulation[29] and experiment.[30] Thermocapillary convection could become unstable as the Marangoni number (Ma) increases.[31] Additionally, the stability of

thermocapillary convection may also be dependent on Pr[32] and the aspect ratio,[33] and the transition route has been revealed in numerical simulation[34] and the earth experiment.[35]

Transient thermocapillary convection is common in nature and industry such as space melting and printing under microgravity.[36] Therefore, dynamical and thermal characteristics of transient thermocapillary convection in a rectangular side-heated top opened cavity have received increasing attention in recent years.[13, 37] It has been demonstrated that a thermal boundary layer (TBL) may form beside the heated sidewall.[38] A surface flow (SF) driven by the thermocapillary force induced by the temperature gradient may occur,[32, 37] and in turn a vertical flow (VF) may also appear owing to the pressure gradient.[39] A series of possible transient flow scenarios and regimes of dynamics and heat transfer have been identified, and corresponding scales of the SF in the cavity have been obtained.[13, 37]

The thermocapillary convection on an inclined plane with a linear temperature distribution has been investigated by e.g. Miladinova *et al*.,[40] Mukhopadhyay and Mukhopadhyay,[41] Chattopadhyay *et al*..[42-44] Further, the thermocapillary convection induced by the surface with a linear temperature distribution is also common in e.g. a laser melting surface, as indicated in Ref. 45 and illustrated in Fig. 1. Moreover, the linear temperature distribution on the surface has also been successfully achieved in the experiment using a lamp and optical system and has been applied for the study of the Marangoni convective flow with a partially contaminated surface.[46, 47] Unfortunately, dynamics and heat transfer of transient thermocapillary convection induced by the surface with a linear temperature distribution are unclear. However, it may be expected that when a linear temperature distribution is suddenly imposed on the surface as performed experimentally in Refs. 46, 47, a distinct stress may be generated on the surface and a thermal boundary layer also appears under the surface, which may in turn induce new dynamical and thermal regimes of transient thermocapillary convection compared to those induced by a sudden heated sidewall.[13, 37] These motivate this study.

In this study, a simple scaling analysis and two-dimensional simulation are adopted, as used in many previous works,[13, 37, 38] to understand the physical mechanism of a transient laminar flow and obtain insights into the evolution of dynamics and heat transfer of transient thermocapillary convection in the cavity with a linear temperature distribution of the liquid surface. That is, the development of transient thermocapillary convection after sudden heating is described; the evolution of dynamics and heat transfer, dependent on e.g. Ma and Pr, is analyzed; the thickness and velocity of the SF and the VF are scaled under different regimes. Further, selected scaling laws are validated by numerical results. The scaling results may be used not only to quantify regimes of dynamics and heat transfer but also directly applied for the estimate of the transient fluid flow in e.g., laser melting, heat pipe and 3D-printing under microgravity.[36]

The remaining parts of the paper are as follows: physical problem is described in Sec. II, scaling analysis is performed in Sec. III, numerical methods are described in Sec. IV, numerical results and validation are presented in Sec. V, and finally, conclusions are summarized in Sec. VI.

Accepted to Phys. Fluids 10.1063/5.0187608

II. PROBLEM DESCRIPTION

We considered a top-opened two-dimensional rectangular cavity, as illustrated in Fig. 1. The width is in the x coordinate of L and the height in the y coordinate of H.

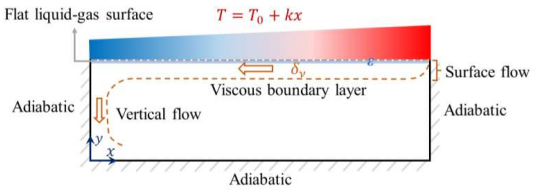

FIG.1. Schematic of thermocapillary convection under a surface of a linear temperature distribution in a rectangular cavity.

The lateral and bottom boundaries are assumed to be non-slip and adiabatic. The top boundary is a liquid-gas surface. Implicit in the analysis below is the assumption that the surface is flat.[37] A linear temperature distribution in the x-direction is suddenly applied for the surface in which the temperature increases from T_0 at the left side toward the right side. The temperature profile may be described as

$$T(x) = T_0 + kx \text{ at } y = H, \tag{1}$$

where k is the temperature gradient factor, which means the temperature increase over the horizontal length:

$$k = \frac{\mathrm{d}T(x)}{\mathrm{d}x}. \tag{2}$$

In the study, k is considered to be positive.

Transient thermocapillary convection in such a cavity may be described by the mass, momentum and energy equations,

$$\frac{\partial u}{\partial x} + \frac{\partial v}{\partial y} = 0, \tag{3}$$

$$\frac{\partial u}{\partial t} + u\frac{\partial u}{\partial x} + v\frac{\partial u}{\partial y} = -\frac{1}{\rho}\frac{\partial p}{\partial x} + \nu\left(\frac{\partial^2 u}{\partial x^2} + \frac{\partial^2 u}{\partial y^2}\right) + F_\alpha, \tag{4}$$

$$\frac{\partial v}{\partial t} + u\frac{\partial v}{\partial x} + v\frac{\partial v}{\partial y} = -\frac{1}{\rho}\frac{\partial p}{\partial y} + \nu\left(\frac{\partial^2 v}{\partial x^2} + \frac{\partial^2 v}{\partial y^2}\right), \tag{5}$$

$$\frac{\partial T}{\partial t} + u\frac{\partial T}{\partial x} + v\frac{\partial T}{\partial y} = \kappa\left(\frac{\partial^2 T}{\partial x^2} + \frac{\partial^2 T}{\partial y^2}\right). \tag{6}$$

Here, F_α denotes thermocapillary force on a surface layer, which may be written as[49]

$$F_\alpha = \frac{1}{\rho}\alpha_T \frac{\partial T}{\partial x}\delta,\ \int_{H-\varepsilon}^{H} \delta dy = 1, \tag{7}$$

where δ is Dirac function, zero out of the surface layer. The thickness of the physical surface layer, denoted as ε, is a time-independent quantity that depends on the properties of the fluid, and is about tens of nanometers[49] with fluctuations of only a few Angstroms.[50]

The working fluid is incompressible Newtonian liquid with constant kinematic viscosity and thermal diffusivity. Note that the variations of density, viscosity and thermal diffusivity with the temperature change play vital role in instability analysis, as demonstrated by Mukhopadhyay *et al*.,[51,52] Chattopadhyay *et al*.[53,54] and Ji *et al*..[55] However, the variations are usually neglected in the study of a steady laminar flow,[13, 39] since the actual variations of e.g., *Ma* and *Pr* are small (smaller than 8% in e.g. silicon oil) in laminar thermocapillary convection. Initially, the fluid is stationary and isothermal at temperature T_0. Boundary conditions in Fig. 1 are assumed as

$$\begin{gathered} u = v = 0 \text{ at } x = 0, L \text{ or } y = 0,\ v = 0 \text{ at } y = H, \\ \frac{\partial T}{\partial x} = 0 \text{ at } x = 0, L \text{ and } \frac{\partial T}{\partial y} = 0 \text{ at } y = 0. \end{gathered} \tag{8}$$

Transient thermocapillary convection is governed mainly by *Ma*, *Pr*, *A* and A_ε, which are given by

$$Ma = \frac{\alpha_T \Delta T L}{\rho \nu \kappa},\ Pr = \frac{\nu}{\kappa},\ A = \frac{H}{L},\ A_\varepsilon = \frac{\varepsilon}{L}, \tag{9}$$

where ΔT is the temperature difference between the highest and lowest temperature on the surface (at the two ends of the cavity). In what follows, a scaling analysis will be applied to Eqs. (3)–(6) to obtain insights into transient laminar thermocapillary convection with the linear temperature distribution on the surface.

III. SCALING ANALYSIS

A. Surface flow

A linear temperature distribution in the *x* direction, when is suddenly applied for the surface of the fluid in a cavity,[46, 47] may generate a nonuniform thermocapillary force in the surface layer, driving the fluid to the cold side. Further, as the momentum diffuses into the cavity by viscous, a horizontal viscous boundary layer, denoted by δ_v, may form below the surface layer, as shown in Fig. 1. Here, the surface layer and viscous boundary layer are hereinafter referred to as the SF.

The SF may be analyzed using (4). It is clear that initially, the advective term is much smaller than the unsteady term. It is noticeable that the advective term is also smaller than the viscous term even over a long time as $Pr > 1$ for most liquids except for molten metal. Thus, the integral of (4) in the *y* direction on the surface layer, which means from

H-ε to H, is denoted as[13, 56]

$$\frac{u}{t}\varepsilon + v\frac{u}{\delta_v} \sim \frac{\alpha_T}{\rho}k. \tag{10}$$

Since ε is very small, δ_v is approximately equal to the thickness of the SF.

The viscous boundary layer is analyzed first to understand the dynamics of the SF. In the horizontal momentum equation (4), the unsteady term is approximately $O(u/t)$, the advective term $O(u^2/L)$ and the viscous term $O(vu/\delta_v^2)$. Note that $O(u^2/L)$ is used to describe the advective term since the first and second advective terms in the momentum equations are on the same order according to the continuity equation. In the initial time, the advective term is much smaller than the unsteady term. Thus, the unsteady term balances the viscous term initially, giving the thickness of the viscous boundary layer,

$$\delta_v \sim Pr^{1/2}\kappa^{1/2}t^{1/2}. \tag{11}$$

Based on (10), the unsteady term is $O(u\varepsilon/t)$ and the viscous term $O(vu/\delta_v)$. Thus, a time scale can be derived from such a balance,

$$t_i \sim \frac{A_c^2 L^2}{Pr\,\kappa}. \tag{12}$$

This means that when $t < t_i$, the SF is under an inertial regime for which the unsteady term balances the thermocapillary term, giving a velocity scale of the SF,

$$u_i \sim \frac{Ma\,Pr\,\kappa^2 t}{L^3 A_c}. \tag{13}$$

When $t > t_i$, the unsteady term in (10) is much smaller than the viscous term, and the SF is under a viscous regime; that is, the viscous term balances the thermocapillary term, which gives a new velocity of the SF,

$$u_v \sim \frac{Ma\,Pr^{1/2}\,\kappa^{3/2}t^{1/2}}{L^2}. \tag{14}$$

The viscous boundary layer grows with time until the cavity is occupied, which means $\delta_v \sim H$. Substituting H into (10), a time scale can be obtained,

$$t_H \sim \frac{A^2 L^2}{Pr\,\kappa}. \tag{15}$$

That is, when $t > t_H$, the viscous term for which the vertical length scale grows from δ_v to H can be express as vu/H. Further, for a sufficiently large time, the SF velocity under a $\delta_v \sim H$ viscous regime develops to a constant value,

$$u_s \sim \frac{Ma\kappa A}{L}. \tag{16}$$

The evolution of the SF velocity is summarized in Fig. 2, and is compared with those in isothermal and uniformly heated situations in Refs. 13 and 37 in the case of Ma = 5000 and Pr = 20. Clearly, the dynamical regimes and velocity scales of the SF in this work are distinct from those in isothermal and uniformly heated situations.

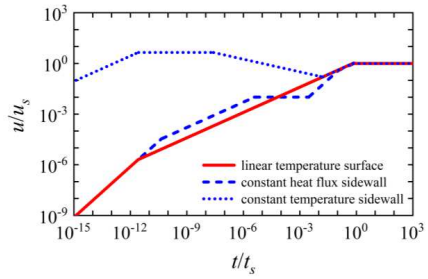

FIG. 2. Evolutions of the SF velocity.[13, 37]

B. Vertical flow

As illustrated in Fig. 1, the SF generates a pressure gradient near the sidewall. Therefore, in the horizontal momentum equation (4), the balance is between the thermocapillary and pressure gradient terms. The integral of Eq. (4) in y direction from $H - \delta_v$ to H is denoted as

$$\frac{p}{\rho \Delta}\delta_v \sim \frac{\alpha_T}{\rho}k, \tag{17}$$

where Δ is the thickness of a vertical boundary layer near the sidewall. Such a pressure rise near the sidewall may further drives a VF near the sidewall. The order of the pressure gradient in the vertical direction may be obtained,

$$\frac{1}{\rho}\frac{\partial p}{\partial y} \sim \frac{p}{\rho v t}. \tag{18}$$

Additionally, based on the conservation of mass, the flow rate may be obtained,

$$Q \sim u\delta_v \sim v\Delta. \tag{19}$$

Notice that the velocity and in turn flow rate of the SF are different under different regimes, which may generate different flow rates of the VF.

1. Viscous-inertial and inertial-inertial regimes

As described in Sec. III. A, the SF is initially governed by the inertial-thermocapillary balance. In fact, for most liquids, the transition time at which the viscous term becomes the same order as the unsteady term described by (12) is smaller than 10^{-9} s. Since the penetration distance of the VF may be scaled with $O(vt)$, substituting (17) into (18), the vertical pressure gradient may be obtained as

$$\frac{1}{\rho}\frac{\partial p}{\partial y} \sim \frac{Ma\,Pr^{1/2}\,\kappa^{3/2}\Delta}{L^2 v t^{3/2}}. \tag{20}$$

Clearly, the velocity scale of the SF governed by the thermocapillary-inertial balance

is u_i, described by (13). Thus, the flow rate scale of the VF can be expressed as

$$Q_i \sim u_i \delta_v \sim \frac{Ma\, Pr^{3/2}\, \kappa^{5/2} t^{3/2}}{L^3 A_\varepsilon}. \tag{21}$$

For the VF, the order of the unsteady term in the vertical momentum equation (5) is $O(v/t)$ and the viscous term is $O(v v/\Delta^2)$. Using (18) and (21), a velocity scale and a thickness scale can be derived at which the viscous term equals to the vertical pressure gradient term,

$$v_{vi} \sim \frac{Ma^{4/5}\, Pr^{4/5}\, \kappa^{8/5} t^{3/5}}{L^{11/5} A_\varepsilon^{3/5}}, \tag{22}$$

$$\Delta_{vi} \sim \frac{Ma^{1/5}\, Pr^{7/10}\, \kappa^{9/10} t^{9/10}}{L^{4/5} A_\varepsilon^{2/5}}. \tag{23}$$

Clearly, in this stage, the SF is under the inertial regime. Thus, the regime for the VF is named as a viscous-inertial regime.

In addition, based on (18) and (21), a balance between the unsteady and pressure gradient term derives velocity and thickness scales of the VF under an inertial-inertial regime,

$$v_{ii} \sim \frac{Ma^{2/3}\, Pr^{2/3}\, \kappa^{4/3} t^{1/3}}{L^{3/5} A_\varepsilon^{1/3}}, \tag{24}$$

$$\Delta_{ii} \sim \frac{Ma^{1/3}\, Pr^{5/6}\, \kappa^{7/6} t^{7/6}}{L^{4/3} A_\varepsilon^{2/3}}. \tag{25}$$

Based on (22) to (25), a time scale can be derived at which the viscous term equals to the unsteady term,

$$\tau_{vi} \sim \frac{L^2 A_\varepsilon}{Ma^{1/2}\, Pr^{1/2}\, \kappa}. \tag{26}$$

This means that the viscous dominance changes to the inertial dominance at the time scaled with (26) for the VF.

It is clear that the ratio of τ_{vi} to t_i is $Pr^{1/2}/(Ma^{1/2} A_\varepsilon)$ based on (12). Thus, the VF near the sidewall rises under the viscous-inertial regime when $t < t_i$ for $Pr/Ma > A_\varepsilon^2$, but under the viscous-inertial regime when $t < \tau_{vi}$ and under the inertial-inertial regime when $\tau_{vi} < t < t_i$ for $Pr/Ma < A_\varepsilon^2$ ($\tau_{vi} < t_i$).

***2. $vt \geq H$* inertial-inertial regime**

As time elapses, the penetration depth vt of the VF reaches H. It can be demonstrated that the VF cannot reach the bottom wall before the viscous dominance changes to the inertial dominance. Using (24), the VF under the inertial-inertial regime reaches the bottom wall in a time scale,

$$\tau_{Hi} \sim \frac{L^2 A^{3/4} A_\varepsilon^{1/4}}{Ma^{1/2}\, Pr^{1/2}\, \kappa}. \tag{27}$$

According to (12), $\tau_{Hi}/t_i \sim Pr^{1/2}A^{3/4}/(Ma^{1/2}A_\varepsilon^{7/4})$. Since $Pr/Ma > A_\varepsilon^{7/2}/A^{3/2}$, $\tau_{Hi} > t_i$. Thus, when the VF reaches the bottom wall, the VF will enter a new stage, which is named as a $vt \geq H$ inertial-inertial regime.

Under the $vt \geq H$ inertial-inertial regime, the penetration depth of the VF is H, and then the scale of the vertical pressure gradient over H can be obtained,

$$-\frac{1}{\rho}\frac{\partial p}{\partial y} \sim \frac{Ma\, Pr^{1/2}\, \kappa^{3/2} \Delta}{L^3 A t^{1/2}}. \tag{28}$$

Repeating the discussion of (22) to (25), based on (28), the velocity scale and the thickness scale can be derived by the equivalent of the inertial term and the vertical pressure gradient term,

$$v_{Hi} \sim \frac{Ma\, Pr\, \kappa^2 t}{L^3 A^{1/2} A_\varepsilon^{1/2}}, \tag{29}$$

$$\Delta_{Hi} \sim \frac{Pr^{1/2}\, \kappa^{1/2} A^{1/2} t^{1/2}}{A_\varepsilon^{1/2}}. \tag{30}$$

Note that due to usually $A > A_\varepsilon$,[13] the inertial term is larger than the viscous term under the $vt \geq H$ inertial-inertial regime until the viscous boundary layer reaches bottom wall

3. Viscous-viscous and inertial-viscous regimes

The SF is under a viscous regime when $t > t_i$. Thus, the volumetric flow rate of the SF is scaled with

$$Q_v \sim u_v\, \delta_v \sim \frac{Ma\, Pr\, \kappa^2\, t}{L^2}. \tag{31}$$

Repeating the discussion of (22) to (25), based on (31), the velocity and the thickness of the VF under a viscous-viscous regime can be obtained,

$$v_{vv} \sim \frac{Ma^{4/5}\, Pr^{1/2}\, \kappa^{13/10} t^{3/10}}{L^{8/5}}. \tag{32}$$

$$\Delta_{vv} \sim \frac{Ma^{1/5}\, Pr^{1/2}\, \kappa^{7/10}\, t^{7/10}}{L^{2/5}}, \tag{33}$$

and under an inertial-viscous regime,

$$v_{iv} \sim \frac{Ma^{2/3}\, Pr^{1/2}\, \kappa^{7/6}\, t^{1/6}}{L^{4/3}}, \tag{34}$$

$$\Delta_{iv} \sim \frac{Ma^{1/3}\, Pr^{1/2}\, \kappa^{5/6}\, t^{5/6}}{L^{2/3}}. \tag{35}$$

Based on (32) to (35), the equivalent of the unsteady term and the viscous term yields a time scale,

$$\tau_{vv} \sim \frac{L^2}{Ma\,\kappa}. \tag{36}$$

That is, (36) is the time scale of the transition between viscous and inertial dominances.

4. $vt \geq H$ inertial-viscous regime

Consider the VF near the sidewall. The time scale for which $vt \sim H$ under a viscous dominance can be given by

$$\tau_{vHv} \sim \frac{L^2 A^{10/13}}{Ma^{8/13}\,Pr^{5/13}\,\kappa}. \tag{37}$$

But the time scale under an inertial dominance can be expressed as

$$\tau_{Hv} \sim \frac{L^2 A^{6/7}}{Ma^{4/7}\,Pr^{3/7}\,\kappa}. \tag{38}$$

Clearly, there is $\tau_{vv} < \tau_{vHv} < \tau_{Hv} < t_H$ for $Pr/Ma < A^2$, implying that the VF does not penetrate through the entire cavity before the balance changes from between the pressure gradient term and the viscous term to between the pressure gradient term and the unsteady term at the time scale τ_{vv}. That is, the VF may develop to the bottom of the cavity under the inertial dominance at the time scale τ_{Hv}, at which time the thickness of the viscous boundary layer has not become H.

Considering both Eqs. (28) and (31), the equivalent between the unsteady term and the pressure gradient term yields the velocity and the thickness of the VF,

$$v_{Hv} \sim \frac{Ma\,Pr^{3/4}\,\kappa^{7/4} t^{3/4}}{L^{5/2} A^{1/2}}, \tag{39}$$

$$\Delta_{Hv} \sim Pr^{1/4}\,A^{1/2} L^{1/2} \kappa^{1/4} t^{1/4}. \tag{40}$$

We can also obtain the velocity and thickness scales under a balance between the viscous term and the pressure gradient term. It is worth noting that the time scale for which the viscous boundary layer reaches the bottom of the cavity equals to the one for which viscous and inertial terms balance. This means that the $vt \geq H$ inertial-viscous regime changes to the $vt \geq H$ and $\delta_v \sim H$ viscous-viscous regime at the time scale t_H.

5. $\delta_v \sim H$ viscous-viscous regime

For $Pr/Ma > A^2$, we have $t_H < \tau_{Hv} < \tau_{vHv} < \tau_{vv}$. That is, the VF does not penetrate through the entire cavity before the thickness of the viscous boundary layer becomes H because of $t_H < \tau_{Hv}$. Further, because of $t_H < \tau_{vv}$, the VF is continuously dominated under a balance between pressure gradient and viscous terms until the viscous boundary layer reaches the bottom of the cavity.

If $\delta_v \sim H$, the vertical pressure gradient term may be obtained as

$$-\frac{1}{\rho}\frac{\partial p}{\partial y} \sim \frac{Ma\,Pr\,\kappa^2 \Delta}{L^3 A v t}. \tag{41}$$

Substituting u_s into Eq. (19), the flow rate is estimated by

$$Q_s \sim u_s H \sim Ma\kappa A^2. \tag{42}$$

Based on Eqs (19), (41) and (42), the velocity and thickness of the VF can be derived by the equivalent between the pressure gradient and viscous terms,

$$v_{vH} \sim \frac{Ma^{4/5}\kappa^{4/5} A}{L^{3/5} t^{1/5}}, \tag{43}$$

$$\Delta_H \sim Ma^{1/5}\kappa^{1/5} A L^{3/5} t^{1/5}. \tag{44}$$

In addition, it may be proved that when $t > t_H$ for $Pr/Ma > A^2$, the VF is continuously dominated by the balance between pressure gradient and viscous terms. Further, the time scale at which the VF reaches the bottom of the cavity is estimated by,

$$\tau_{HH} \sim \frac{L^2}{Ma\kappa}. \tag{45}$$

6. $vt \geq H$ and $\delta_v \sim H$ viscous-viscous regime

It is clear that the penetration depth of the VF is H under the $vt \geq H$ and $\delta_v \sim H$ viscous-viscous regime, the pressure gradient term is estimated by

$$-\frac{1}{\rho}\frac{\partial p}{\partial y} \sim \frac{Ma\,Pr\,\kappa^2 \Delta}{L^4 A^2}. \tag{46}$$

Further, based on Eqs. (42) and (46), the velocity and thickness of the VF are scaled with

$$v_{HH} \sim \frac{Ma\kappa A}{L}, \tag{47}$$

$$\Delta_{HH} \sim AL. \tag{48}$$

In fact, it can be demonstrated that the viscous term is always greater than the inertial term under the $vt \geq H$ and $\delta_v \sim H$ the viscous-viscous regime.

In addition, according to different time scales, four possible evolution scenarios of the VF may be summarized and are plotted in Table I and Fig. 3.

TABLE I. VF under different regimes in different evolution scenarios.

Evolution scenario		Time	Velocity	Regime
VF I	$Pr/Ma < A_c^{7/2}/A^{3/2}$	$t < \tau_{vi}$	$v_{vi} \sim \frac{Ma^{4/5}\,Pr^{4/5}\,\kappa^{8/5} t^{3/5}}{L^{11/5} A_c^{3/5}}$	Viscous - inertial

		$\tau_{vi} < t < \tau_{Hi}$	$v_{ii} \sim \frac{Ma^{2/3}\, Pr^{2/3}\, \kappa^{4/3} t^{1/3}}{L^{3/5} A_\varepsilon^{1/3}}$	Inertial - inertial
		$\tau_{Hi} < t < t_i$	$v_{Hi} \sim \frac{Ma\, Pr\, \kappa^2 t}{L^3 A^{1/2} A_\varepsilon^{1/2}}$	$vt \geq H$ inertial - inertial
		$t_i < t < t_H$	$v_{Hv} \sim \frac{Ma\, Pr^{3/4}\, \kappa^{7/4} t^{3/4}}{L^{5/2} A^{1/2}}$	$vt \geq H$ inertial - viscous
		$t > t_H$	$v_{HH} \sim \frac{Ma\kappa A}{L}$	$vt \geq H$ viscous - $\delta_v \sim H$ viscous
VF II	$A_\varepsilon^{7/2}/A^{3/2} < Pr/Ma < A_\varepsilon^2$	$t < \tau_{vi}$	$v_{vi} \sim \frac{Ma^{4/5}\, Pr^{4/5}\, \kappa^{8/5} t^{3/5}}{L^{11/5} A_\varepsilon^{3/5}}$	Viscous - inertial
		$\tau_{vi} < t < t_i$	$v_{ii} \sim \frac{Ma^{2/3}\, Pr^{2/3}\, \kappa^{4/3} t^{1/3}}{L^{3/5} A_\varepsilon^{1/3}}$	Inertial - inertial
		$t_i < t < \tau_{vv}$	$v_{vv} \sim \frac{Ma^{4/5}\, Pr^{1/2}\, \kappa^{13/10} t^{3/10}}{L^{8/5}}$	Viscous - viscous
		$\tau_{vv} < t < \tau_{Hv}$	$v_{iv} \sim \frac{Ma^{2/3}\, Pr^{1/2}\, \kappa^{7/6} t^{1/6}}{L^{4/3}}$	Inertial - viscous
		$\tau_{Hv} < t < t_H$	$v_{Hv} \sim \frac{Ma\, Pr^{3/4}\, \kappa^{7/4} t^{3/4}}{L^{5/2} A^{1/2}}$	$vt \geq H$ inertial - viscous
		$t > t_H$	$v_{HH} \sim \frac{Ma\kappa A}{L}$	$vt \geq H$ viscous - $\delta_v \sim H$ viscous
VF III	$A_\varepsilon^2 < Pr/Ma < A^2$	$t < t_i$	$v_{vi} \sim \frac{Ma^{4/5}\, Pr^{4/5}\, \kappa^{8/5} t^{3/5}}{L^{11/5} A_\varepsilon^{3/5}}$	Viscous - inertial
		$t_i < t < \tau_{vv}$	$v_{vv} \sim \frac{Ma^{4/5}\, Pr^{1/2}\, \kappa^{13/10} t^{3/10}}{L^{8/5}}$	Viscous - viscous
		$\tau_{vv} < t < \tau_{Hv}$	$v_{iv} \sim \frac{Ma^{2/3}\, Pr^{1/2}\, \kappa^{7/6} t^{1/6}}{L^{4/3}}$	Inertial - viscous
		$\tau_{Hv} < t < t_H$	$v_{Hv} \sim \frac{Ma\, Pr^{3/4}\, \kappa^{7/4} t^{3/4}}{L^{5/2} A^{1/2}}$	$vt \geq H$ inertial - viscous
		$t > t_H$	$v_{HH} \sim \frac{Ma\kappa A}{L}$	$vt \geq H$ viscous - $\delta_v \sim H$ viscous

		$t < t_i$	$v_{vi} \sim \frac{Ma^{4/5}\, Pr^{4/5}\, \kappa^{8/5} t^{3/5}}{L^{11/5} A_c^{3/5}}$	Viscous - inertial
VF IV	$Pr/Ma > A^2$	$t_i < t < t_H$	$v_{vv} \sim \frac{Ma^{4/5}\, Pr^{1/2}\, \kappa^{13/10} t^{3/10}}{L^{8/5}}$	Viscous - viscous
		$t_H < t < \tau_{HH}$	$v_{vH} \sim \frac{Ma^{4/5} \kappa^{4/5} A}{L^{3/5} t^{1/5}}$	Viscous - $\delta_v \sim H$ viscous
		$t > \tau_{HH}$	$v_{HH} \sim \frac{Ma\kappa A}{L}$	$vt \geq H$ viscous - $\delta_v \sim H$ viscous

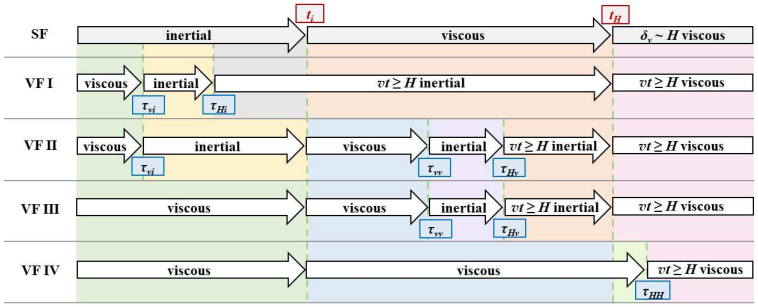

FIG. 3. Regimes of VF (in VFs I-IV).

C. Thermal boundary layer

It may be expected that when a linear temperature distribution is suddenly applied for the surface, heat may be transferred into the fluid in the cavity by conduction, resulting in a horizontal TBL beneath the surface. The energy equation (6) may describe heat transfer between the surface and the interior fluid. The unsteady term, convection term and conductive term in Eq. (6) are approximately $O(\Delta T/t)$, $O(v\Delta T/H)$ and $O(\kappa\Delta T/\delta_T^2)$, respectively, where δ_T is the thickness of the TBL. Clearly, for a sufficiently small time, the convective term is negligible in comparison with the conductive term. That is, there is a balance mainly between the unsteady term and the conductive term, yielding a scale for the thickness of the TBL,

$$\delta_{Ti} \sim \kappa^{1/2} t^{1/2}. \tag{49}$$

The SF may horizontally convect heat away. As time goes on, the convective term becomes larger and even exceeds the unsteady term. For $t < t_i$, if the ratio of convective to unsteady terms is unity, a time can be obtained,

$$t_t \sim \frac{A_c^{1/2} L^2}{Ma^{1/2}\, Pr^{1/2}\, \kappa}. \tag{50}$$

Clearly, $t_i < t_t$ for $Pr/Ma > A_\varepsilon^3$, but $t_i > t_t$ for $Pr/Ma < A_\varepsilon^3$. Since usually $A_\varepsilon < 10^{-5}$ (see, e.g., Ref. 13). and in case of $Ma > 10^6$, instability or even chaos may occur in thermocapillary convection,[49, 57, 58] the case for only $Pr/Ma > A_\varepsilon^3$ is considered in this study.

For $t > t_i$, over the velocity scale u_v, the above comparison yields a new time scale for the switch from the unsteady-conductive balance to the convective-conductive balance, which is given by

$$t_t \sim \frac{L^2}{Ma^{3/2}\, Pr^{1/3}\, \kappa}. \tag{51}$$

Based on (51), there exist $t_t < t_H$ for $Pr/Ma < A^3$ but $t_H < t_t$ for $Pr/Ma > A^3$. Accordingly, in what follows, the evolution scenarios with different regimes will be analyzed.

In the evolution scenario for $Pr/Ma < A^3$ ($t_t < t_H$), the transition from the unsteady-conductive balance to the convective-conductive balance occurs before the viscous boundary layer reaches the bottom wall.

When $t < t_t$, the convective term $O(uk)$ is insignificant in comparison with the unsteady term $O(\Delta T/t)$ in the energy equation (6), and the TBL develops under the balance of unsteady and conductive terms with a thickness scale of δ_{Ti} in (49).

The convective term becomes large and the unsteady term may be negligible when $t_t < t < t_H$. The SF moves with a velocity of u_v under a balance between thermocapillary and viscous terms. A thickness scale can be derived by the energy balance between convective and conductive terms,

$$\delta_{Tv} \sim \frac{L^{3/2}}{Ma^{1/2}\, Pr^{1/4}\, \kappa^{1/4} t^{1/4}}. \tag{52}$$

When $t > t_H$, the thermocapillary term is balanced by the viscous term for which δ_v grows to H with a velocity scale of u_s (10). Inserting u_s into the energy equation (6), a thickness scale is obtained,

$$\delta_{Ts} \sim \frac{L}{Ma^{1/2} A^{1/2}}. \tag{53}$$

This means that the TBL reaches the steady stage and the thickness remains constant. Moreover, it may be verified that the TBL will reach the steady state before the viscous layer reaches the bottom of the cavity for $Pr/Ma < A^3$ due to $t_t < t_H$.

Heat transfer between the SF and the interior fluid may be scaled with $O(\lambda\Delta T/\delta_T)$, where λ denotes thermal conductivity. Further, the Nusselt number (Nu) for $Pr/Ma < A^3$ may be obtained by normalizing the heat flux using $\lambda\Delta T/H$ based on (49), (52) and (53), respectively,

$$Nu \sim \begin{cases} \dfrac{L}{\kappa^{1/2} t^{1/2}}, 0 < t < t_t, \\ \dfrac{Ma^{1/2}\, Pr^{1/4}\, \kappa^{1/4} t^{1/4}}{L^{1/2}}, t_t < t < t_H, \\ Ma^{1/2} A^{1/2}, t > t_H. \end{cases} \tag{54}$$

In the evolution scenario for $Pr/Ma > A^3$, we have $t_H < t_t$. That is, the viscous boundary layer fills the cavity with the velocity scale of u_s before the convective term becomes dominant. Further, based on the energy equation (6), a balance between the inertial term and the convective term yields a time scale,

$$t_{ts} \sim \frac{L^2}{MaA\kappa}. \tag{55}$$

Since convection is very weak when $t < t_{ts}$, the TBL grows as time increases in which the inertial-conductive balance dominates the SF with a thickness scale (49). When $t > t_{ts}$, the TBL maintains a constant thickness (53).

It is noteworthy that the TBL is distinct when only $\delta_T < H$, which yields a criterion,

$$Ma > \frac{1}{A^3}. \tag{56}$$

That is, the TBL is distinct if (56) is satisfied. Further, based on (49) and (53), heat transfer through the SF for $Pr/Ma > A^3$ may be expressed as

$$Nu \sim \begin{cases} \dfrac{L}{\kappa^{1/2} t^{1/2}}, 0 < t < t_{ts}, \\ Ma^{1/2} A^{1/2}, t > t_{ts}. \end{cases} \tag{57}$$

The evolution scenarios of the horizontal TBL with the thickness scales under different regimes are presented in Table II. Further, the thickness is also shown in Fig. 4 under different regimes for $Pr/Ma < A^3$ and $Pr/Ma < A^3$. Evolution scenarios of the TBL and VF are shown in the *Ma–Pr–A* space in Fig. 5.

TABLE II. Thickness of TBL under different regimes in different evolution scenarios.

Evolution scenario		Time	Thickness	Regime
TBL I	$Pr/Ma < A^3$	$t < t_t$	$\delta_{Ti} \sim \kappa^{1/2} t^{1/2}$	Inertial-conductive
		$t_t < t < t_H$	$\delta_{Tv} \sim \dfrac{L^{3/2}}{Ma^{1/2}\, Pr^{1/4}\, \kappa^{1/4} t^{1/4}}$	Viscous-convective
		$t > t_H$	$\delta_{Ts} \sim \dfrac{L}{Ma^{1/2} A^{1/2}}$	$\delta_v \sim H$ viscous-convective
TBL II	$Pr/Ma > A^3$	$t < t_{ts}$	$\delta_{Ti} \sim \kappa^{1/2} t^{1/2}$	Inertial-conductive
		$t > t_{ts}$	$\delta_{Ts} \sim \dfrac{L}{Ma^{1/2} A^{1/2}}$	$\delta_v \sim H$ viscous-convective

Accepted to Phys. Fluids 10.1063/5.0187608

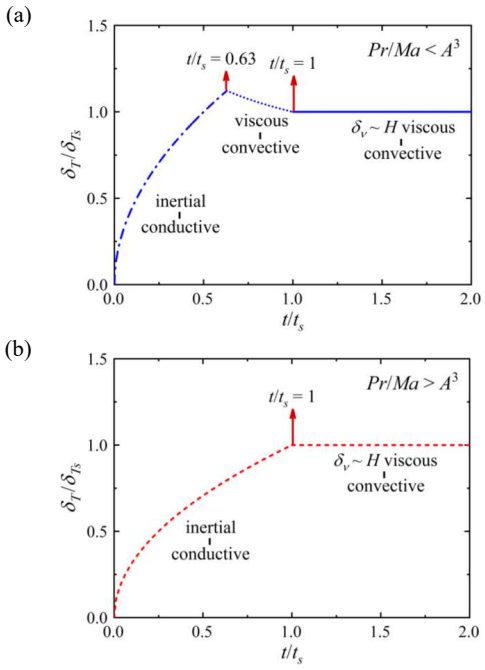

FIG. 4. Thickness of TBL for Ma = 5000 in two evolution scenarios. Here, $t_s = t_H$ in (a), given by Eq. (15) in TBL I for $Pr/Ma < A^3$, but $t_s = t_{ts}$ in (b), given by Eq. (51) in TBL II for $Pr/Ma > A^3$.

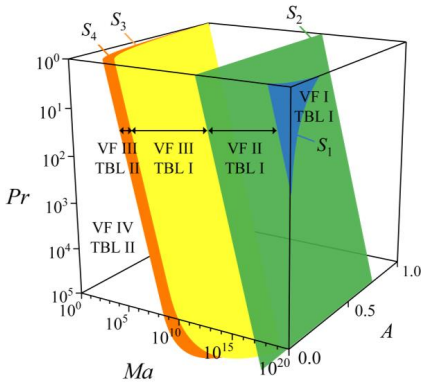

FIG. 5. Evolution scenarios of TBL and VF in *Ma*-*Pr*-*A* space. Here, S_1: $Pr = MaA_\varepsilon^{7/2}/A^{3/2}$, S_2: $Pr = MaA_\varepsilon^2$, S_3: $Pr = MaA^3$, and S_4: $Pr = MaA^2$.

IV. NUMERICAL METHOD

2D numerical simulation may be used to characterize transient thermocapillary

convection, since the two-dimensional numerical results of the thermocapillary convective flow agrees well with the experimental ones.[48, 59] For convenience, the 2D governing equations (3)–(6) were simplified to non-dimensional forms by x/x^*, y/y^*, δ/δ^* and $\varepsilon/\varepsilon^* \sim L$, $t/t^* \sim L^2/(Ma\kappa)$, $T^* \sim (T - T_0)/\Delta T$, u/u^* and $v/v^* \sim Ma\kappa/L$ and $p/p^* \sim \rho Ma^2\kappa^2/L^2$, as described in Ref. 13.

Figure 6 illustrates the computational domain and boundary conditions. The top boundary was at a linear temperature distribution and imposed by a constant Marangoni stress. The other wall boundaries of the computational domain were considered to be adiabatic and no slip. All boundaries were considered to be rigid. Initially, the fluid in the domain was motionless and isothermal at a zero non-dimensional temperature. Previous studies[13, 37] have demonstrated that thermocapillary convection in a rectangular cavity can be described well by the numerical simulations with Marangoni stress on the non-deformable flat surface.

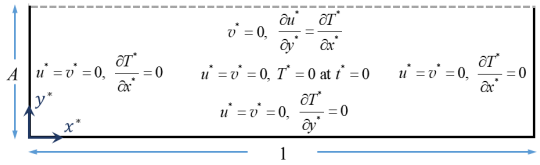

FIG. 6. Schematic of boundary conditions in the computational domain.

The numerical method to solve governing equations has been described and experimentally verified in previous studies.[13, 37] Since there is no experimental result of transient thermocapillary convection in a rectangular pool under a surface of a linear temperature distribution in the literature, the further verification with the experiment has not been conducted in this study.

Four different meshes were used for the mesh sensitivity test with finer cells toward the surface and boundaries. For example, the computational cells expand vertically at a fixed rate toward the bottom of the cavity from the size 1×10^{-5}, 8×10^{-6}, 4×10^{-6} and 2.5×10^{-6} to the size 4×10^{-5}, 2×10^{-5}, 2×10^{-5} and 1×10^{-5}, respectively.

The largest Marangoni number of $Ma = 250000$ in the present numerical cases was adopted in the mesh sensitivity test. The numerical results show that the flow in this study is steady for $Ma \leq 250000$ and even low Prandtl number (e.g., =10), which is different from that in a cavity with the isothermal lateral wall (also see Ref. 13). The results have been listed in TABLE III. To ensure the accuracy of numerical results and to keep the computing cost, a mesh of 100 × 300 was used in this study for which the velocity and temperature difference calculated with a finer mesh was less than 3%.

TABLE III. Mesh dependency test.

A	Ma	Mesh $H \times L$	Steady u^* at fixed point (0.5, 0.5A) (%)	Steady T^* at fixed point (0.8, 0.9A) (%)

1/5	250000	50×150	0.010244801(10.55%)	0.34820(6.19%)
1/5	250000	71×210	0.010605483(7.39%)	0.35058(5.54%)
1/5	250000	100×300	0.011452625	0.37116
1/5	250000	200×600	0.011403985(0.42%)	0.36023(2.94%)

In fact, the numerical results obtained using the present procedures were compared with the experimental results in Ref. 13 in which two types of results are consistent. That is, the present procedures are applied for the description of thermocapillary convection in the cavity.

V. NUMERICAL RESULTS AND VALIDATION

To present the physics of transient thermocapillary convection flows under different regimes and validate the scaling relations derived from Sec. III, 2D numerical simulation was conducted for a fixed aspect ratio (A = 0.2) but for Pr from 2 to 2×10^3 (corresponding to silicone oils from 0.65cs to 200cs) and Ma from 2500 to 250000, which cover all regimes.

A. Flow structure

Figure 7 plots the streamlines and isotherms for Ma = 2500. In a short time after sudden heating, the isotherms are approximately parallel to each other owing to heat conduction, as shown in Fig. 7(a). As time goes, the thickness of the TBL increases and the isotherms slightly contorts in the right corner, as shown in Fig. 7(b). As time increases further, the region occupied by the hotter fluid continuously enlarges from the right top corner to the left bottom corner, as shown in Figs. 7(c) and 7(d). Additionally, the streamlines in Fig. 7 shows that there exists a distinct large circulation driven by the thermocapillary force. However, the further examination of numerical results shows that transient thermocapillary convection is still weak under conduction dominance for such a small Ma.

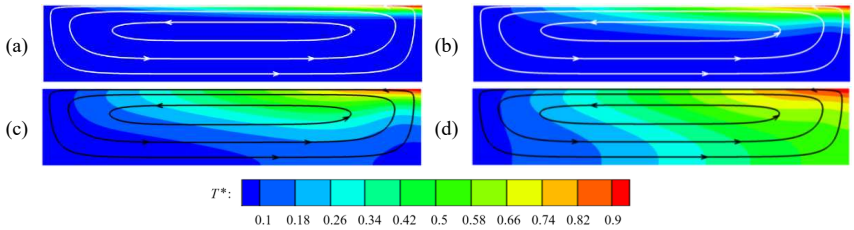

FIG. 7. Streamlines and isotherms from 0.1 to 0.9 with an interval between two neighbouring isotherms being 0.08 at different times for Pr = 200 and Ma = 2500. (a) At t^*/t_{ts}^*=0.14. (b) At t^*/t_{ts}^*=0.85. (c) At t^*/t_{ts}^*=3.61. (d) At t^*/t_{ts}^*=57.30.

As *Ma* increases, convection becomes stronger. Figure 8 shows the streamlines and isotherms for *Ma* = 250000. The SF is distinct and drives a VF, as shown in Fig. 8(a). Further, a back flow from the left to the right becomes stronger with time and a circulation is clear in the cavity, as shown in Fig. 8(b). As time goes, the circulation develops until the developed stage, as shown in Figs. 8(c)-(f). Moreover, it is clear that the symmetry of the circulation about the vertical middle line is lost with increase of the *Ma*, as shown in Figs. 7 and 8.

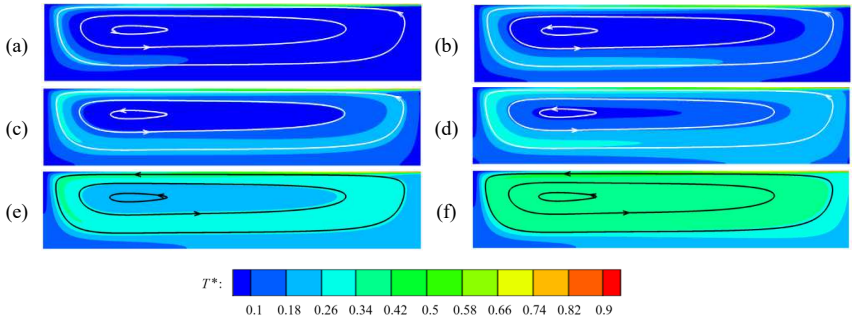

FIG. 8. Streamlines and isotherms from 0.1 to 0.9 with an interval between two neighbouring isotherms being 0.08 at different times for *Pr* = 200 and *Ma* = 250000. (a) At t^*/t_H^*= 0.95. (b) At t^*/t_H^*=3.71. (c) At t^*/t_H^*=5.29. (d) At t^*/t_H^*=8.13. (e) At t^*/t_H^*=16.03. (f) At t^*/t_H^*=110.76.

B. Verification of scaling laws

According to the analysis in Sec. III, by sudden heating the surface with a linear temperature distribution, a SF can be generated under a thermocapillary force. The velocity of the SF may be different under different regimes. For validation of the scaling law (14) under viscous regime, the velocity for the SF was extracted at $x^* = 0.5$ and $y^* = A$. Here, the non-dimensional format is adopted (also for all following figures). Figure 9 shows the velocity normalized by (14). A good linear correlation between $u_v^* A^{-1}$ and $(t^*/t_H^*)^{1/2}$ can be distinguished, indicating that the scaling law (14) is verified.

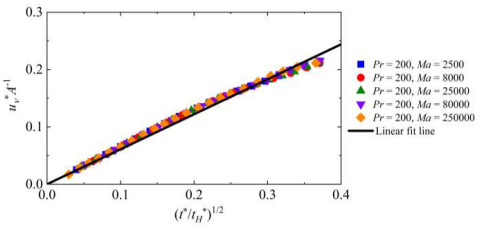

FIG. 9. Velocity of SF under viscous regime.

For a sufficiently large time, the velocity of the SF becomes constant, as indicated in (16). To validate the velocity scale of (16), the velocity was calculated at $x^* = 0.5$ and $y^* = A$ on the surface. According to (16), the normalized velocity u_s^* is independent of Ma, which may be found in Fig. 10. This confirms that the scaling prediction (16) is working.

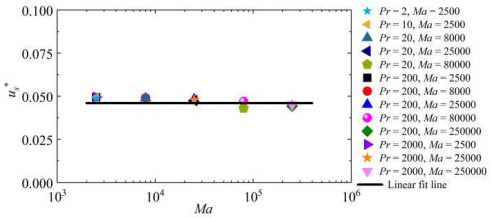

FIG. 10. Velocity of SF under $\delta_v \sim H$ viscous regime.

As described above, a VF near the sidewall may be generated by the pressure gradient induced by the SF. The analysis in Sec. III. B shows that the VF may travel at different velocity scales under different regimes. When $\tau_{Hv} < t < t_H$, the VF travels at a velocity of (39) under the $vt \geq H$ inertial-viscous regime in VFs I-III. In simulation results, the velocity of the VF is measured by the maximum vertical velocity at $y^* = 0.5A$. Figure 11 shows the velocity of the VF normalized by (39). A good linear correlation between $v_{Hv}^* A^{-1}$ and $(t^*/t_H^*)^{3/4}$ can be distinguished, suggesting that the scaling prediction is able to predict the VF under the $vt \geq H$ inertial-viscous regime in VFs I-III. However, it is clear that data slightly scatter as time increases owing to the presence of the bottom wall.

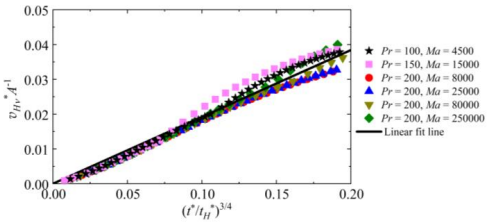

FIG. 11. Velocity of VF under $vt \geq H$ inertial-viscous regime in VFs I-III.

In order to verify the velocity of the VF under the $vt \geq H$ and $\delta_v \sim H$ viscous- viscous regime in VFs I-IV, the maximum vertical velocity at $y^* = 0.5A$ was measured. Figure 12 shows the velocity of the VF normalized by (47). Clearly, the velocity is independent of Ma, indicating that the scaling law (47) can describe the VF under the $vt \geq H$ and $\delta_v \sim H$ viscous-viscous regime.

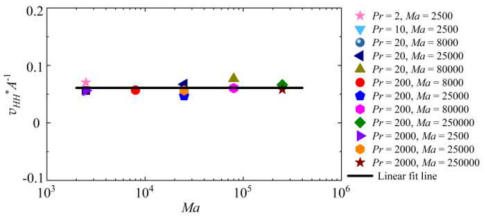

FIG. 12. Velocity of VF under $vt \geq H$ and $\delta_v \sim H$ viscous-viscous regime in VFs I-IV.

For validation of the scaling law (40), we also measured the thickness of the VF under the $vt \geq H$ inertial-viscous regime in VFs I-III based on the numerical solutions, defined as the horizontal distance from the left wall to the interior edge of the VF for which $v = 0.0004$ at $y^* = 0.5A$. The numerical results are plotted in Fig. 13. It is seen from this figure that $\Delta_{Hv}{}^{*}A^{-1}$ is proportional to $(t^*/t_H{}^{*})^{1/4}$, which confirms the scaling law (40).

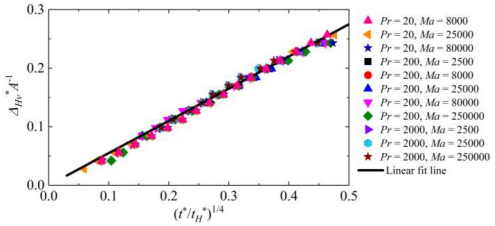

FIG. 13. Thickness of VF under $vt \geq H$ inertial-viscous regime in VFs I-III.

As time goes on, the thickness of the VF becomes a constant, which is independent of Ma, as described by (48). Figure 14 shows $\Delta_{HH}{}^{*}$ extracted from numerical results. The thickness predicted in (48) is independent of Ma, which confirms the scaling prediction in (48). Here, the thickness for $Ma = 5000$ and 8000 slightly deviates the scaling prediction because there is the circulation flow in the cavity.

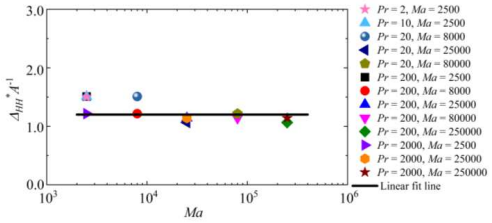

FIG. 14. Thickness of VF under $vt \geq H$ and $\delta_v \sim H$ viscous-viscous regime in VFs I-IV.

Scaling analysis indicates that as soon as the linear temperature distribution is applied, heat transfer can occur, resulting in the formation of a TBL beneath the top boundary, as scaled with (49). The thickness of the TBL in numerical results was measured as the length from surface to the isotherm of $T^* = 0.3$ at $x^* = 0.5$, at which the disturbance from the circulation of the convective flow may be reduced.[13] To validate (49), the thickness was calculated from numerical results in TBLs I and II, respectively. Figure 15 shows the thickness and time normalized by (49). Clearly, $\delta_{Ti}{}^* Ma^{1/3} A^{1/6}$ has a clear linear function of $(t^*/t_t{}^*)^{1/2}$ and $\delta_{Ti}{}^* Ma^{1/2} A^{1/2}$ has a perfect linear function of $(t^*/t_{ts}{}^*)^{1/2}$ under the inertial-conductive regime in TBLs I and II, respectively, implying that the proposed scaling law (49) is confirmed.

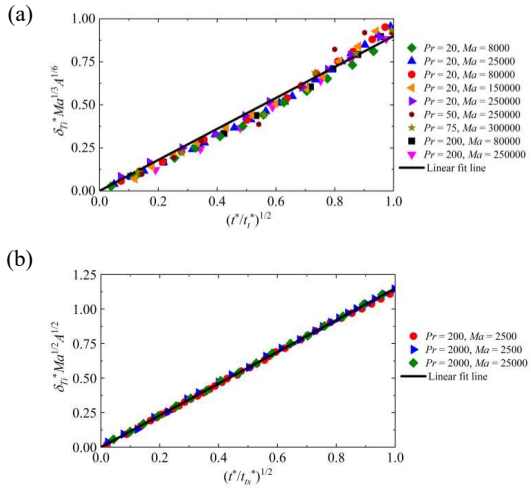

FIG. 15. Thickness of TBL under inertial-conductive regime in TBLs I (a) and II (b).

To validate the thickness scale (52), the normalized thickness under the convective-viscous regime in TBL I was measured from numerical results and is plotted in Fig. 16. Clearly, $\delta_{Tv}{}^* Ma^{1/2} A^{1/2}$ is proportional to $(t^*/t_H{}^*)^{-1/4}$, suggesting that the scaling law (52) may describe the thickness scale under convective-viscous regime in TBL I.

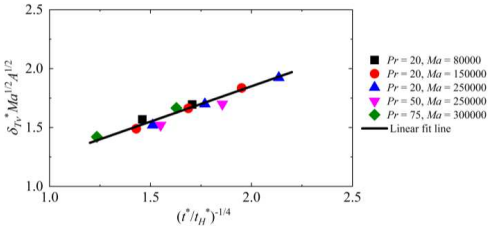

FIG. 16. Thickness of TBL under viscous-convective regime in TBL I.

During the unsteady stage, the thickness of the TBL may change as time elapses, as precited by the scale of (49) and (52). Further, the scaling analysis shows that the TBL may reach the steady stage with a constant thickness in both TBLs I and II, which is described by the scale of (53). To verify (53), the thickness of TBL under the $\delta_v \sim H$ viscous-convective regime was measured. As seen from Fig. 17, there is an approximately linear relation of $\delta_{T_S}^* A^{1/2}$ and $Ma^{-1/2}$. Generally, there is agreement between the scaling prediction in (53) and numerical results. Note that the thickness for Ma = 8000 deviates the scaling prediction because the circulation flow adjacent to the sidewall disturbs.

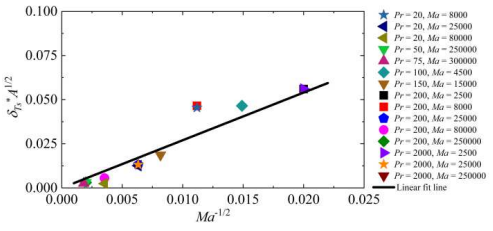

FIG. 17. Thickness of TBL under $\delta_v \sim H$ viscous-convective regime in TBLs I and II.

Heat transfer near the surface can be quantified by the Nusselt number Nu, which is predicted in (54). To verify (54), the Nusselt number of the surface with the linear temperature distribution was calculated from the numerical results. Figure 18 shows the Nusselt number in unsteady stage. Clearly, there is a perfect linear relation between $NuMa^{-1/2}A^{-1/2}$ and $(t^*/t_t^*)^{1/2}$, which confirms the scaling law of heat transfer (54) under the inertial-conductive regime in TBL I well.

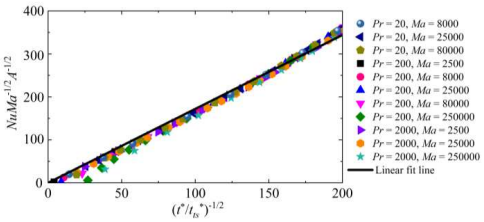

FIG. 18. Nusselt number of the surface with linear temperature distribution under inertial-conductive regime in TBL I.

Furthermore, the Nusselt number of the surface with the linear temperature distribution in the steady stage Nu was also measured and is plotted in Fig. 19. There is a good linear relation between Nu and $Ma^{1/2}A^{1/2}$, which further verifies (54) and (57) under the $\delta_v \sim H$ viscous-convective regime in TBLs I and II.

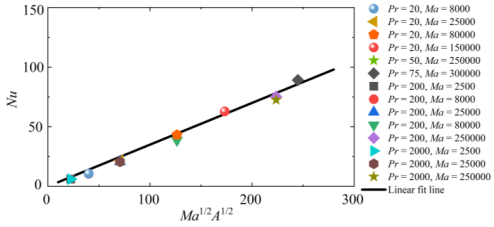

FIG. 19. Nusselt number of the surface with linear temperature distribution under $\delta_v \sim H$ viscous-convective regime in TBLs I and II.

VI. CONCLUSIONS

A discussion based on scaling analysis and numerical simulations for transient thermocapillary convection under a surface of a linear temperature distribution in a rectangular cavity at a zero-gravity condition is presented. A set of scaling laws of velocity and thickness has been derived by scaling analysis to describe heat transfer and dynamics of thermocapillary convection under different regimes in different evolutions. The scaling relationships describe very complex interactions between the SF, VF, TBL and viscous boundary layer in the cavity.

Further, 2D numerical simulation has been performed to characterize the physics of transient flow and to verify representative scaling relations. The velocity and thickness of the SF and VF, and the Nu of the surface measured from numerical results are in accord with scaling predictions. Therefore, the present scaling results may describe the transient thermocapillary convection flows induced by a surface of a linear temperature distribution, and in turn estimate the flow and heat transfer (e.g., the velocity of the SF $u_v \sim MaPr^{1/2}\kappa^{3/2}t^{1/2}/L^2$, the Nusselt number of the surface $Nu \sim Ma^{1/2}A^{1/2}$) in industrial applications.

ACKNOWLEDGMENTS

The authors would like to thank the National Natural Science Foundation of China (12302349) for the financial support.

AUTHOR DECLARATIONS

Conflict of Interest

The authors have no conflicts to disclose.

Author Contributions

Xinyuan Meng: Conceptualization (equal); Formal analysis (equal); Investigation (equal); Methodology (equal); Writing – original draft (lead).
Enhui Chen: Conceptualization (equal); Formal analysis (equal); Funding acquisition (lead); Investigation (equal); Methodology (supporting); Writing - original draft (supporting); Writing - review and editing (supporting).
Feng Xu: Conceptualization (equal); Formal analysis (equal); Investigation (supporting); Methodology (equal); Project administration (lead); Writing - original draft (supporting); Writing - review and editing (lead).

DATA AVAILABILITY

Data will be made available on request.

REFERENCES

[1] S. C. Hardy, "The motion of bubbles in a vertical temperature gradient," J. Colloid Interface Sci. **69**, 157 (1979).

[2] D. Villers, and J. K. Platten, "Marangoni convection in systems presenting a minimum in surface tension," PhysicoChem. Hydrodyn. **6**, 435 (1985).

[3] L. E. Scriven, and C. V. Sternling, "The Marangoni effects," Nature **187**, 186 (1960).

[4] J. Srinivasan, and B. Basu, "A numerical study of thermocapillary flow in a rectangular cavity during laser melting," Int. J. Heat Mass Transfer **29**, 563 (1986).

[5] H. Minakuchi, Y. Okano, and S. Dost, "A three-dimensional numerical simulation study of the Marangoni convection occurring in the crystal growth of Si_xGe_{1-x} by the float-zone technique in zero gravity," J. Cryst. Growth **266**, 140 (2004).

[6] M. Xia, D. Gu, G. Yu, D. Dai, H. Chen, and Q. Shi, "Selective laser melting 3D printing of Ni-based superalloy: Understanding thermodynamic mechanisms," Sci. Bull. **61**, 1013 (2016).

[7] S. H. Jin, S. N. Dunham, J. Song, X. Xie, J.-h. Kim, C. Lu, A. Islam, F. Du, J. Kim, J. Felts, Y. Li, F. Xiong, M. A. Wahab, M. Menon, E. Cho, K. L. Grosse, D. J. Lee, H. U. Chung, E. Pop, M. A. Alam, W. P. King, Y. Huang, and J. A. Rogers, "Using nanoscale thermocapillary flows to create arrays of purely semiconducting single-walled carbon nanotubes," Nat. Nanotechnol. **8**, 347 (2013).

[8] F. N. Piñan Basualdo, A. Bolopion, M. Gauthier, and P. Lambert, "A microrobotic platform actuated by thermocapillary flows for manipulation at the air-water interface," Sci. Robot. **6**, 3557 (2021).

[9] K. Hu, S. Zheng, and Q. Chen, "The response to external excitations in thermocapillary liquid layers," Phys. Fluids **33**, 032104 (2021).

[10] A. H. Saifi, V. M. Mundhada, and M. K. Tripathi, "Thermocapillary convection in liquid-in-liquid capillary bridges due to a heating/cooling ring," Phys. Fluids **34**, 032112 (2022).

[11] T. Watanabe, Y. Kowata, and I. Ueno, "Flow transition and hydrothermal wave instability of

thermocapillary-driven flow in a free rectangular liquid film," Int. J. Heat Mass Transfer **116**, 635 (2018).
[12] Q. Kang, D. Wu, L. Duan, L. Hu, J. Wang, P. Zhang, and W. Hu, "The effects of geometry and heating rate on thermocapillary convection in the liquid bridge," J. Fluid Mech **881**, 951 (2019).
[13] E. Chen, and F. Xu, "Transient Marangoni convection induced by an isothermal sidewall of a rectangular liquid pool," J. Fluid Mech **928**, A6 (2021).
[14] W. Liu, P. G. Chen, J. Ouazzani, and Q. Liu, "Thermocapillary flow transition in an evaporating liquid layer in a heated cylindrical cell," Int. J. Heat Mass Transfer **153**, 119587 (2020).
[15] J. Chen, C. Wu, Y. Li, and J. Yu, "Capillary ratio dependence of thermal-solutal capillary convection in a shallow annular pool with radial temperature and concentration gradients," Int. J. Therm. Sci. **139**, 15 (2019).
[16] X. Zhou, Y. Jiang, Y. Hou, and M. Du, "Thermocapillary convection instability in annular two-layer system under various gravity levels," Microgravity Sci. Technol. **31**, 641 (2019).
[17] Z.-B. Wu, and W.-R. Hu, "Thermocapillary migration of a planar droplet at moderate and large Marangoni numbers," Acta Mech. **223**, 609 (2012).
[18] K.-X. Hu, C.-Y. Yan, and Q.-S. Chen, "Instability of thermocapillary–buoyancy convection in droplet migration," Phys. Fluids **31**, 122101 (2019).
[19] H. Liu, J. He, Z. Zeng, and Z. Qiu, "Instabilities of thermocapillary-buoyancy flow in a rotating annular pool for medium-Prandtl-number fluid," Phys. Rev. E **104**, 035101 (2021).
[20] T.-S. Wang, and W.-Y. Shi, "Transition of Marangoni convection instability patterns during evaporation of sessile droplet at constant contact line mode," Int. J. Heat Mass Transfer **148**, 119138 (2020).
[21] C. Li, N. Zhang, X. Wang, and X. Ye, "Marangoni instability of an evaporating binary mixture droplet," Phys. Fluids **35**, 084103 (2023).
[22] Q. Yang, B. Q. Li, X. Lv, F. Song, Y. Liu, and F. Xu, "Mathematical modelling of thermocapillary patterning in thin liquid film: An equilibrium study," J. Fluid Mech **919**, A29 (2021).
[23] N. Martínez Figueira, P. Salgado Sánchez, A. Bello, K. Olfe, and J. Rodríguez, "Effect of surface heat exchange on phase change materials melting with thermocapillary flow in microgravity," Phys. Fluids **35**, 084115 (2023).
[24] I. I. Ryzhkov, and V. M. Shevtsova, "Thermocapillary instabilities in liquid columns under co – and counter-current gas flows," Int. J. Heat Mass Transfer **55**, 1236 (2012).
[25] Q. Yang, Y. Liu, X. Jia, T. Zhang, and F. Song, "Numerical study of the thermocapillary instability in a thin liquid–air film," Phys. Fluids **34**, 092117 (2022).
[26] X. Zhou, F. Chi, Y. Jiang, and Q. Chen, "Moderate Prandtl number nanofluid thermocapillary convection instability in rectangular cavity," Microgravity Sci. Technol. **34**, 24 (2022).
[27] C. Peromingo, D. Gligor, P. Salgado Sánchez, A. Bello, and K. Olfe, "Sloshing reduction in microgravity: Thermocapillary-based control and passive baffles," Phys. Fluids **35**, 102114 (2023).
[28] Z. Chen, Y. Li, and J. Zhan, "Double-diffusive Marangoni convection in a rectangular cavity: Onset of convection," Phys. Fluids **22**, 034106 (2010).
[29] W. Hu, Z. Tang, and K. Li, "Numerical study on onset of oscillatory thermocapillary flow in rectangular liquid pool," Sci. China: Technol. Sci. **53**, 1069 (2010).
[30] M. Sakurai, J. Leypoldt, H. C. Kuhlmann, H. J. Rath, and A. Hirata, "Pattern formation and transient thermocapillary flow in a rectangular side-heated open cavity," Microgravity Sci. Technol. **13**, 30 (2002).
[31] C. Jyh-Chen, and H. Farn-Shiun, "Oscillatory thermocapillary flow in a rectangular cavity," Int. J. Heat Mass Transfer **36**, 3743 (1993).
[32] M. K. Smith, and S. H. Davis, "Instabilities of dynamic thermocapillary liquid layers. Part 1.

Convective instabilities," J. Fluid Mech **132**, 119 (1983).

[33] X. Zhou, and X. Huai, "Thermosolutocapillary convection in an open rectangular cavity with dynamic free surface," J. Heat Transfer **137**, (2015).

[34] Y.-S. Li, Z. Chen, and J. Zhan, "Double-diffusive Marangoni convection in a rectangular cavity: Transition to chaos," Int. J. Heat Mass Transfer **53**, 5223 (2010).

[35] H. Jiang, L. Duan, and Q. Kang, "A peculiar bifurcation transition route of thermocapillary convection in rectangular liquid layers," Exp. Therm. Fluid Sci. **88**, 8 (2017).

[36] P. S. Wei, C. L. Lin, H. J. Liu, and C. N. Ting, "Transient thermocapillary convection in a molten or weld pool," J. Manuf. Sci. Eng. **134**, (2012).

[37] E. Chen, and F. Xu, "Transient thermocapillary convection flows in a rectangular cavity with an evenly heated lateral wall," Phys. Fluids **33**, 013602 (2021).

[38] J. Patterson, and J. Imberger, "Unsteady natural convection in a rectangular cavity," J. Fluid Mech **100**, 65 (1980).

[39] A. K. Sen, and S. H. Davis, "Steady thermocapillary flows in two-dimensional slots," J. Fluid Mech **121**, 163 (1982).

[40] S. Miladinova, S. Slavtchev, G. Lebon, and J.-C. Legros, "Long-wave instabilities of non-uniformly heated falling films," J. Fluid Mech **453**, 153 (2002).

[41] A. Mukhopadhyay, and A. Mukhopadhyay, "Stability of conducting viscous film flowing down an inclined plane with linear temperature variation in the presence of a uniform normal electric field," Int. J. Heat Mass Transfer **52**, 709 (2009).

[42] S. Chattopadhyay, A. Mukhopadhyay, A. K. Barua, and A. K. Gaonkar, "Thermocapillary instability on a film falling down a non-uniformly heated slippery incline," Int. J. Non-Linear Mech. **133**, 103718 (2021).

[43] S. Chattopadhyay, "Thermocapillary instability in the presence of uniform normal electric field: effect of odd viscosity," J. Eng. Math. **131**, 9 (2021).

[44] S. Chattopadhyay, "Falling liquid film down a non-uniformly heated slippery inclined plane with odd viscosity effects," Int. J. Heat Mass Transfer **218**, 124807 (2024).

[45] T. L. Bergman, and B. W. Webb, "Simulation of pure metal melting with buoyancy and surface tension forces in the liquid phase," Int. J. Heat Mass Transfer **33**, 139 (1990).

[46] A. V. Shmyrov, A. I. Mizev, V. A. Demin, M. I. Petukhov, and D. A. Bratsun, "Phase transitions on partially contaminated surface under the influence of thermocapillary flow," J. Fluid Mech **877**, 495 (2019).

[47] A. Shmyrov, A. Mizev, V. Demin, M. Petukhov, and D. Bratsun, "On the extent of surface stagnation produced jointly by insoluble surfactant and thermocapillary flow," Adv. Colloid Interface Sci. **255**, 10 (2018).

[48] Y. Kamotani, S. Ostrach, and A. Pline, "A Thermocapillary Convection Experiment in Microgravity," J. Heat Transfer 117, 611 (1995).

[49] G. Tryggvason, R. Scardovelli, and S. Zaleski, *Direct Numerical Simulations of Gas–Liquid Multiphase Flows* (Cambridge University Press, Cambridge, 2011).

[50] P. G. de Gennes, F. Brochard Wyart, and D. Quéré, *Capillarity and Wetting Phenomena: Drops, Bubbles, Pearls, Waves* (Springer, New York, 2013).

[51] A. Mukhopadhyay, and S. Chattopadhyay, "Long wave instability of thin film flowing down an inclined plane with linear variation of thermophysical properties for very small Biot number," Int. J. Non-Linear Mech. **100**, 20 (2018).

[52] A. Mukhopadhyay, S. Chattopadhyay, and A. K. Barua, *Effects of Strong Viscosity with Variable Fluid Properties on Falling Film Instability* (Springer International Publishing, Cham, 2022).
[53] S. Chattopadhyay, "Odd-viscosity-induced instability of a thin film with variable density," Phys. Fluids **33**, 082102 (2021).
[54] S. Chattopadhyay, P. Boragunde, A. K. Gaonkar, A. K. Barua, and A. Mukhopadhyay, "Falling liquid films on a slippery substrate with variable fluid properties," Int. J. Non-Linear Mech. **147**, 104200 (2022).
[55] H. Ji, C. Falcon, E. Sedighi, A. Sadeghpour, Y. S. Ju, and A. L. Bertozzi, "Thermally-driven coalescence in thin liquid film flowing down a fibre," J. Fluid Mech **916**, A19 (2021).
[56] G. K. Batchelor, *An Introduction to Fluid Dynamics* (Cambridge University Press, Cambridge, 2000).
[57] D. Schwabe, and J. Metzger, "Coupling and separation of buoyant and thermocapillary convection," J. Cryst. Growth **97**, 23 (1989).
[58] P. Salgado Sánchez, J. M. Ezquerro, J. Fernández, and J. Rodríguez, "Thermocapillary effects during the melting of phase-change materials in microgravity: Steady and oscillatory flow regimes," J. Fluid Mech **908**, A20 (2021).
[59] D. Villers, and J. Platten, "Coupled buoyancy and Marangoni convection in acetone: Experiments and comparison with numerical simulations," J. Fluid Mech **234**, 487 (1992).